symmetry

MDPI

Article

A Flux-Limited Model for Glioma Patterning with Hypoxia-Induced Angiogenesis

Pawan Kumar † **and Christina Surulescu** *,†

Felix-Klein-Zentrum für Mathematik, TU Kaiserslautern, 67663 Kaiserslautern, Germany; kumar@mathematik.uni-kl.de

* Correspondence: surulescu@mathematik.uni-kl.de

† Current address: Felix-Klein-Zentrum für Mathematik, Paul-Ehrlich-Str. 31, 67663 Kaiserslautern, Germany.

Received: 22 September 2020; Accepted: 10 November 2020; Published: 13 November 2020

Abstract: We propose a model for glioma patterns in a microlocal tumor environment under the influence of acidity, angiogenesis, and tissue anisotropy. The bottom-up model deduction eventually leads to a system of reaction–diffusion–taxis equations for glioma and endothelial cell population densities, of which the former infers flux limitation both in the self-diffusion and taxis terms. The model extends a recently introduced (Kumar, Li and Surulescu, 2020) description of glioma pseudopalisade formation with the aim of studying the effect of hypoxia-induced tumor vascularization on the establishment and maintenance of these histological patterns which are typical for high-grade brain cancer. Numerical simulations of the population level dynamics are performed to investigate several model scenarios containing this and further effects.

Keywords: glioblastoma; pseudopalisades; hypoxia-induced angiogenesis; flux-limited diffusion and taxis; kinetic transport equations; equilibrium-based moment closure

1. Introduction

Classification of glioma, the most common type of primary brain tumors, typically comprises four grades, according to the degree of malignancy [1,2]. The highest grade, IV (which includes the most aggressive type, glioblastoma multiforme, abbreviated as GBM), corresponds to characteristic histological patterns called pseudopalisades; they exhibit garland-like hypercellular structures surrounding necrotic regions usually centered around one or several sites of vaso-occlusion [3–6], and they are associated with poor patient survival prognosis [1].

More specifically, vascular occlusion and thrombosis [3,5] result in hypoxia, which promotes migration of glioma cells away from the highly acidic area, as well as tissue necrotization therein. Hypoxia around the pseudopalisading cells triggers the process of capillary formation, which involves a cascade of coordinated steps [7,8]. It typically starts with tumor cells overexpressing hypoxia-inducible regulators of angiogenesis, including vascular endothelial growth factor (VEGF) [4]. The latter acts as a chemoattractant and proliferation promotor for endothelial cells (ECs) lining the surrounding blood vessels. The chemotactic migration of ECs towards VEGF gradients is accompanied by formation of new capillaries off existing ones, thus leading to microvascular hyperplasia, which is common in GBM [4,9] and which facilitates the growth of the neoplasm [4]. Understanding the mechanisms of tumor malignancy can contribute to development and tuning of therapeutic strategies, e.g., by targeting angiogenesis [10] or by tumor alkalization [11] used in a (neo)adjuvant way to other approaches (such as surgery and radiotherapy).

There is a large amount of literature concerning the mathematical modeling of the development of glioma spread; we refer to [12–14] for some reviews. Among the few mathematical models explicitly addressing glioma pseudopalisade formation (we refer to [15,16] for agent-based approaches and to [17–19] for continuous descriptions), the latter proposed a multiscale approach for deducing a reaction–(myopic) diffusion equation with repellent pH-taxis for glioma cell density coupled with a reaction–diffusion partial differential equation (PDE) for the acidity (expressed as proton concentration) produced by tumor cells. The derivation of this system started with describing the evolution of the glioma distribution function on the mesoscopic scale in the kinetic theory of active particles (KTAP) framework [20]; thereby, the activity variable represented the amount of glioma transmembrane units occupied with protons. A parabolic scaling led to the announced reaction–diffusion–taxis (RDT) equation on the so-called macroscopic level of the glioma population, including in its terms influences of acidity and tissue coming from the lower modeling scales. (In the sequel, we will use the term "macroscopic" to designate quantities that depend only on time and space, not to be confounded with the true biological size scale on which pseudopalisades are observed and which is, in that acception, microscopic. Thus, in the following, "microscopic" means single-cell level, while "mesoscopic" refers to distributions of cells depending on time, space, and further kinetic and/or activity variables.) The two equations for glioma and acidity were capable of qualitatively reproducing pseudopalisade-like patterns. In this work, we aim to use a related approach and to extend the model in [17] such as to account for hypoxia-triggered angiogenesis and its effects on the pseudopalisade patterns. We thereby continue in the line of previous works [21–31] dealing with cancer cell migration in heterogeneous tissues. The deduced macroscopic system is able to generate the expected patterns; indeed, accounting for angiogenic effects leads to disruption of the garland-like structure of glioma pseudopalisades and transient behavior as consequences of proton uptake and nutrient supply by ECs forming capillaries. Another novel feature of this model is the flux limitation obtained in the macroscopic terms describing diffusion and repellent pH-taxis. The modeling approach has similarities to [25,32]; however, the passage from the mesoscopic to the macrolevel follows a different path. We provide more comments on this issue in Sections 2 and 4.

The rest of the paper is structured as follows: Section 2 is dedicated to setting up the micro-meso formulation in the KTAP framework and to deduce a macroscopic system of differential equations characterizing the dynamics of glioma density (RDT) with flux-limited diffusion and repellent pH-taxis, EC density (RDT) with linear diffusion and chemotaxis toward VEGF gradients, and concentrations of acidity and VEGF (both with linear diffusion and tumor- and EC-dependent source terms). In Section 3, we perform numerical simulations for various scenarios of the macroscopic model obtained in Section 2 and interpret the results. Finally, in Section 4, we provide a discussion and an outlook on further problems of interest in this context.

2. Modeling

Since the behavior of glioma cells as a pattern-forming population is influenced by processes taking place on single-cell and mesoscopic (featuring velocity-dependent cell density; the direction of cell migration in response to the underlying tissue structure seems to be relevant for the shape and extent of the patterns) levels, we consider a multiscale approach in which we start from such lower scale descriptions and then deduce (in a formal way) the macroscopic dynamics leading to the mentioned patterns. (We refer to [33] for a recent review of principle-based modeling in a broader context involving such mathematical structures.) We begin by introducing some notations for the various variables and functions involved in our modeling process:

- variables: time $t \geq 0$, position $\mathbf{x} \in \mathbb{R}^N$, velocity of glioma cells $\mathbf{v} \in V = s\mathbb{S}^{N-1} \subset \mathbb{R}^N$, velocity of ECs $\boldsymbol{\vartheta} \in \Theta = \sigma\mathbb{S}^{N-1} \subset \mathbb{R}^N$; we assume the cell speeds $s, \sigma > 0$ to be constant; $\mathbb{S}^{N-1}$ denotes the unit sphere in $\mathbb{R}^N$;
- $\hat{\mathbf{v}} = \frac{\mathbf{v}}{|\mathbf{v}|}$, $\hat{\boldsymbol{\vartheta}} = \frac{\boldsymbol{\vartheta}}{|\boldsymbol{\vartheta}|}$ are unit vectors denoting the directions of vectors $\mathbf{v} \in V$ and $\boldsymbol{\vartheta} \in \Theta$, respectively;

- $p(t,\mathbf{x},\mathbf{v})$: (mesoscopic) density function of glioma cells and $M(t,\mathbf{x}) = \int_V p(t,\mathbf{x},\mathbf{v})d\mathbf{v}$: macroscopic density of glioma;
- $w(t,\mathbf{x},\boldsymbol{\vartheta})$: (mesoscopic) density function of ECs and $W(t,\mathbf{x}) = \int_\Theta w(t,\mathbf{x},\boldsymbol{\vartheta})d\boldsymbol{\vartheta}$: macroscopic density of ECs.
- $q(\mathbf{x},\boldsymbol{\theta})$: (known) directional distribution function of tissue fibers with orientation $\theta \in \mathbb{S}^{N-1}$. It holds that $\int_{\mathbb{S}^{N-1}} q(\mathbf{x},\boldsymbol{\theta})d\boldsymbol{\theta} = 1$; for $\omega = \int_V q(\mathbf{x},\hat{\mathbf{v}})d\mathbf{v} = s^{N-1}$, it holds then that $\int_V \frac{q(\mathbf{x},\hat{\mathbf{v}})}{\omega}d\mathbf{v} = 1$;
- $\mathbb{E}_q(\mathbf{x}) := \int_{\mathbb{S}^{N-1}} \boldsymbol{\theta} q(\mathbf{x},\boldsymbol{\theta})d\boldsymbol{\theta}$: mean fiber orientation. We also denote $\tilde{\mathbb{E}}_q(\mathbf{x}) := \int_V \mathbf{v}\frac{q(\mathbf{x},\hat{\mathbf{v}})}{\omega}d\mathbf{v}$ and call it mean fiber direction;
- $\mathbb{V}_q(\mathbf{x}) := \int_{\mathbb{S}^{N-1}} (\boldsymbol{\theta} - \mathbb{E}_q(\mathbf{x})) \otimes (\boldsymbol{\theta} - \mathbb{E}_q(\mathbf{x}))q(\mathbf{x},\boldsymbol{\theta})d\boldsymbol{\theta}$: variance–covariance matrix for orientation distribution of tissue fibers, and, correspondingly, $\tilde{\mathbb{V}}_q(\mathbf{x}) = \int_V (\mathbf{v} - \tilde{\mathbb{E}}_q(\mathbf{x})) \otimes (\mathbf{v} - \tilde{\mathbb{E}}_q(\mathbf{x}))\frac{q(\mathbf{x},\hat{\mathbf{v}})}{\omega}d\mathbf{v}$;
- $h(t,\mathbf{x})$: concentration of protons (acidity), a macroscopic quantity;
- $g(t,\mathbf{x})$: concentration of VEGF, also a macroscopic quantity;
- $\lambda > 0$: constant glioma turning rate;
- $\eta(\boldsymbol{\vartheta}, g(t,\mathbf{x})) > 0$: EC turning rate.

2.1. Glioma Cells

In the spirit of [23], we consider single cell (microscale) dynamics in the form

$$\frac{d\mathbf{x}}{dt} = \mathbf{v}, \quad \frac{d\mathbf{v}}{dt} = -\alpha \mathbf{S}(\mathbf{v},h,M), \tag{1}$$

with

$$\begin{aligned}\mathbf{S}(\mathbf{v},h,M) &= \mathbb{B}(\mathbf{v})\left(\gamma_1 \frac{\nabla h}{\sqrt{K_h^2/X^2 + |\nabla h|^2}} + \gamma_2 \frac{\nabla M}{\sqrt{K_M^2/X^2 + |\nabla M|^2}}\right) \\ &=: \mathbb{B}(\mathbf{v})\boldsymbol{\phi}(h,M),\end{aligned} \tag{2}$$

where $\gamma_1, \gamma_2 \geq 0$ are weighting constants, $K_h, K_M, X > 0$ are further dimensional constants (to be explained below, with X to be chosen in Section 3.1), and the tensor $\mathbb{B}(\mathbf{v}) := |\mathbf{v}|^2\mathbb{I}_N - \mathbf{v}\otimes\mathbf{v}$ models biomechanical cell stress; thereby, $\mathbf{v}\otimes\mathbf{v}$ represents active cell stress, while $-|\mathbf{v}|^2\mathbb{I}_N$ is the isotropic part. Hence, similarly to [21,23,25], the velocity (and, in particular, the direction) of glioma cells is also influenced by a weighted sum of gradients (each inferring some limitation); increasing gradients of proton concentration have a repelling effect, and the cells also try to avoid crowded regions. The constant $\alpha > 0$ in (1) is a scaling parameter influenced by the gradients of h and M; for further details, we refer to [23]. Notice that Equation (1) actually implies $\frac{d|\mathbf{v}|^2}{dt} = 0$, which is in line with our assumption of the cell speed $s = |\mathbf{v}|$ being constant.

Correspondingly, under the usual assumption of the particles (cells) whose trajectories are described in Equation (1) being independent and identically distributed, on the mesoscale, we have the following kinetic transport equation (KTE) for the evolution of the glioma cell distribution function $p(t,\mathbf{x},\mathbf{v})$:

$$\nabla_{(t,\mathbf{x},\mathbf{v})} \cdot ((1,\mathbf{v},-\alpha\mathbf{S}(\mathbf{v},h,M))p) = p_t + \nabla_\mathbf{x}\cdot(\mathbf{v}p) - \alpha\nabla_\mathbf{v}\cdot(\mathbf{S}(\mathbf{v},h,M)p) = \mathcal{L}[\lambda]p + \mathcal{P}(M,h,W), \tag{3}$$

where $\mathcal{L}[\lambda]p(t,\mathbf{x},\mathbf{v}) = -\lambda p(t,\mathbf{x},\mathbf{v}) + \lambda\int_V K(\mathbf{v},\mathbf{v}')p(t,\mathbf{x},\mathbf{v}')d\mathbf{v}'$ is a turning operator with constant turning rate $\lambda > 0$ and turning kernel K giving the likelihood of cells having velocity $\mathbf{v}'$ to adopt a new velocity regime $\mathbf{v}$. As in [29] and many subsequent works [17,22–24,26,28], we choose $K(\mathbf{v},\mathbf{v}') := \frac{q(\mathbf{x},\theta)}{\omega}$, meaning that the reorientation of cells is due to contact guidance by tissue, the latter having orientation distribution q. Hence, $\mathcal{L}[\lambda]p(t,\mathbf{x},\mathbf{v}) = \lambda(M\frac{q(\mathbf{x},\hat{\mathbf{v}})}{\omega} - p(t,\mathbf{x},\mathbf{v}))$. Moreover, as in [23], we assume p to be compactly supported in the velocity space.

The term $\mathcal{P}(M,h,W)$ models glioma cell proliferation, which is supposed to depend on the amount of cells already present (irrespective of their orientation) and on favorable (nutrients provided by

ECs of density W) and unfavorable (acidity h) factors in the environment. More detailed descriptions account for proliferative interactions mediated by kernels depending on kinetic or activity variables, as in [23,28], or even differentiate between moving and proliferating cells [27,31]. Here, we would rather focus on the macrolevel influences and choose a uniform velocity kernel to characterize such interactions, i.e.,

$$\begin{aligned}\mathcal{P}(M,h,W) &= \left(1-\frac{M}{K_M}\right)\int_V \left(\mu_1\left(1-\frac{h}{K_h}\right)+\mu_2\frac{W/K_W}{1+W/K_W}\right)\frac{1}{|V|}p(t,\mathbf{x},\mathbf{v}')d\mathbf{v}' \\ &= \frac{\mu_1}{|V|}M\left(1-\frac{M}{K_M}\right)\left(1-\frac{h}{K_h}\right)+\frac{\mu_2}{|V|}M\frac{W/K_W}{1+W/K_W},\end{aligned} \tag{4}$$

where $\mu_1, \mu_2 > 0$ are rates related to the cell growth or decay due to acidity and ECs. The positive constants K_M and K_W represent carrying capacities of glioma and endothelial cells, respectively, while $K_h > 0$ denotes a threshold of proton concentration, which, when exceeded, leads to glioma cell death. Similarly to [17], we consider a logistic type growth (as long as the environment is not overly acidic) supplemented by a limited (excessive hyperplasia does not lead to further glioma proliferation due to space limitation) growth due to the interaction with ECs here representing the nutrient-supplying vasculature.

In [17], a parabolic upscaling was used (with the observation that a hyperbolic one leads to a PDE which is too much drift-dominated and not able to reproduce pseudopalisade patterns) to deduce a macroscopic equation for the dynamics of macroscopic glioma density M from the KTE formulation; the microscale dynamics in that setting focused on the evolution of an activity variable quantifying the amount of transmembrane units occupied by protons. In [23], where velocity dynamics akin to Equation (1) was considered (without limitations, however, as in the denominators of $\mathbf{S}$), parabolic scaling led to the reaction–diffusion–taxis PDE for glioma evolution of the macroscale. Instead, we will consider here a moment closure approach similar to that in [21,30], ensuring the closure by way of an equilibrium distribution.

For that purpose, we introduce the following quantities:

$$(M\mathbf{U})(t,\mathbf{x}) := \int_V \mathbf{v}p(t,\mathbf{x},\mathbf{v})d\mathbf{v}, \tag{5}$$

$$\mathbb{P}(t,\mathbf{x}) := \int_V (\mathbf{v}-\mathbf{U}(t,\mathbf{x}))\otimes(\mathbf{v}-\mathbf{U}(t,\mathbf{x}))\,p(t,\mathbf{x},\mathbf{v})d\mathbf{v}, \tag{6}$$

commonly designated as momentum and pressure tensor, respectively. Thereby, $\mathbf{U}$ represents the so-called ensemble (macroscopic) cell velocity.

Integrating Equation (3) w.r.t. $\mathbf{v}$, we get

$$\partial_t M + \nabla_{\mathbf{x}}\cdot(M\mathbf{U}) = \mu_1 M\left(1-\frac{M}{K_M}\right)\left(1-\frac{h}{K_h}\right)+\mu_2 M\frac{W/K_W}{1+W/K_W}. \tag{7}$$

Multiplying Equation (3) by $\mathbf{v}$ and integrating again w.r.t. $\mathbf{v}$, we get

$$\partial_t(M\mathbf{U}) + \nabla_{\mathbf{x}}\cdot\int_V \mathbf{v}\otimes\mathbf{v}pd\mathbf{v} + \alpha\int_V \mathbf{S}(\mathbf{v},h,M)pd\mathbf{v} = \lambda M(\tilde{\mathbb{E}}_q - \mathbf{U}). \tag{8}$$

From Equation (6),

$$\mathbb{P} = \int_V \mathbf{v}\otimes\mathbf{v}\;pd\mathbf{v} - M\mathbf{U}\otimes\mathbf{U},$$

hence, due to Equation (2), we can rewrite Equation (8) as

$$\partial_t(M\mathbf{U}) + \nabla_x\cdot(\mathbb{P}+M\mathbf{U}\otimes\mathbf{U}) - \alpha(\mathbb{P}+M\mathbf{U}\otimes\mathbf{U}-s^2M\mathbb{I}_N)\boldsymbol{\phi}(h,M) = \lambda M(\tilde{\mathbb{E}}_q-\mathbf{U}). \tag{9}$$

System (8), (9) is not closed, since the pressure tensor $\mathbb{P}$ involves a second order moment of p and is therefore unknown. In order to close the system, we proceed as in [30] and assume that it is close to equilibrium, which also dominates the second order moments. If we also assume that, at equilibrium, we can neglect cell proliferation (as it indeed happens much slower than the motility-related processes), then, in virtue of Equation (3), we can write

$$p_{\text{equil}} = \frac{q}{\omega} M, \tag{10}$$

which also leads to

$$\mathbf{U}_{\text{equil}} = \frac{1}{M} \int_V \mathbf{v} p_{\text{equil}} d\mathbf{v} = \tilde{\mathbb{E}}_q \tag{11}$$

and

$$\mathbb{P}_{\text{equil}} = \int_V (\mathbf{v} - \tilde{\mathbb{E}}_q) \otimes (\mathbf{v} - \tilde{\mathbb{E}}_q) \frac{q}{\omega} M d\mathbf{v} = M \tilde{\mathbb{V}}_q, \tag{12}$$

hence, at equilibrium, the momentum of glioma population is driven by the cell ensemble aligning their motion to the average fiber orientation $\tilde{\mathbb{E}}_q$, and the population pressure is generated by the variance–covariance matrix of the orientation distribution q/ω of tissue surrounding the cells.

Thus, we get from Equation (9)

$$\partial_t (M\mathbf{U}) + \nabla_{\mathbf{x}} \cdot (M\mathbf{U} \otimes \mathbf{U}) = -\nabla_{\mathbf{x}} \cdot \mathbb{P}_{\text{equil}} + \alpha \left(\mathbb{P}_{\text{equil}} + M\mathbf{U} \otimes \mathbf{U} - s^2 M \mathbb{I}_N \right) \boldsymbol{\phi}(h, M) + \lambda (M \tilde{\mathbb{E}}_q - M\mathbf{U}). \tag{13}$$

The middle term on the right hand side of Equation (13) stems from the description of forces acting on the cells; we suppose that the tensor $M\mathbf{U} \otimes \mathbf{U}$ therein is itself relating to the equilibrium situation, and thus replacing it by $M\tilde{\mathbb{E}}_q \otimes \tilde{\mathbb{E}}_q$. On the other hand, the left side in Equation (13) can be interpreted as directional derivative of the momentum $M\mathbf{U}$ in the direction $\mathbf{U}$ of the cell flow. As in [30], we consider that the cell flux relaxes quickly to its equilibrium, so that

$$M\mathbf{U} = M\tilde{\mathbb{E}}_q - \frac{1}{\lambda} \nabla_{\mathbf{x}} \cdot \mathbb{P}_{\text{equil}} + \frac{\alpha}{\lambda} \left(\mathbb{P}_{\text{equil}} + M\tilde{\mathbb{E}}_q \otimes \tilde{\mathbb{E}}_q - s^2 M \mathbb{I}_N \right) \boldsymbol{\phi}(h, M). \tag{14}$$

If, furthermore, we assume that the tissue is undirected (as suggested by the simulation results in [17]), this translates into $\tilde{\mathbb{E}}_q = \mathbf{0}$, which simplifies the above expression of the momentum:

$$M\mathbf{U} = -\nabla_{\mathbf{x}} \cdot (\mathbb{D}_T(\mathbf{x}) M) + \alpha (\mathbb{D}_T(\mathbf{x}) - \frac{s^2}{\lambda} \mathbb{I}_N) M \boldsymbol{\phi}(h, M), \tag{15}$$

with $\mathbb{D}_T(\mathbf{x}) := \frac{1}{\lambda} \int_V \mathbf{v} \otimes \mathbf{v} \frac{q(\mathbf{x}, \hat{\mathbf{v}})}{\omega} d\mathbf{v}$ denoting, as in previous works (e.g., [17,26]), the so-called tumor diffusion tensor.

Plugging Equation (15) into Equation (7) then leads to the macroscopic PDE for glioma evolution

$$\partial_t M = \nabla\nabla : (\mathbb{D}_T M) + \alpha \nabla \cdot \left(\left(\tfrac{s^2}{\lambda} \mathbb{I}_N - \mathbb{D}_T \right) \boldsymbol{\phi}(h, M)\, M \right) + \mu_1 M \left(1 - \tfrac{M}{K_M} \right) \left(1 - \tfrac{h}{K_h} \right) + \mu_2 \tfrac{MW/K_W}{1 + W/K_W}, \tag{16}$$

which is, of course, merely an approximation, in view of the many assumptions made above.

The myopic diffusion term in Equation (16) is made of a drift and a classical diffusion term:

$$\nabla\nabla : (\mathbb{D}_T M) = \nabla \cdot (\nabla \cdot \mathbb{D}_T\, M) + \nabla \cdot (\mathbb{D}_T \nabla M),$$

hence, using the expression of $\boldsymbol{\phi}(h, M)$, we can rewrite Equation (16) in the form of a PDE in which both self-diffusion (first term in Equation (17)) and repellent pH-taxis (third term in Equation (17)) are (at least partially) flux-limited:

$$\begin{aligned}\partial_t M =& \nabla \cdot \left(\left(\mathbb{D}_T + \alpha\gamma_2 \left(\frac{s^2}{\lambda}\mathbb{I}_N - \mathbb{D}_T \right) \frac{M}{\sqrt{K_M^2/X^2 + |\nabla M|^2}} \right) \nabla M \right) + \nabla \cdot (\nabla \cdot \mathbb{D}_T\, M) \\ &+ \nabla \cdot \left(\alpha\gamma_1 \left(\frac{s^2}{\lambda}\mathbb{I}_N - \mathbb{D}_T \right) M \frac{\nabla h}{\sqrt{K_h^2/X^2 + |\nabla h|^2}} \right) + \mu_1 M \left(1 - \frac{M}{K_M}\right)\left(1 - \frac{h}{K_h}\right) + \mu_2 \frac{MW/K_W}{1 + W/K_W}.\end{aligned} \tag{17}$$

Notice that, in order to have a genuine repellent pH-taxis, the tensor $\frac{s^2}{\lambda}\mathbb{I}_N - \mathbb{D}_T$ should be positive definite, which also ensures a nondegenerating, proper diffusion (without being, however, a necessary condition). Under the hypothesis of undirected tissue, i.e., for $\mathbb{E}_q = \mathbf{0}$, this amounts to $\mathbb{I}_N - \mathbb{V}_q = \mathbb{I}_N - \int_{\mathbb{S}^{N-1}} \boldsymbol{\theta} \otimes \boldsymbol{\theta} q(\boldsymbol{\theta}) d\boldsymbol{\theta}$ being positive definite. This is, for instance, the case if q is the so-called peanut distribution [34]:

$$q(\mathbf{x}, \boldsymbol{\theta}) = \frac{N}{|\mathbb{S}^{N-1}|\ \mathrm{trace}\ \mathbb{D}_{water}(\mathbf{x})} \boldsymbol{\theta}^T \mathbb{D}_{water}(\mathbf{x}) \boldsymbol{\theta},$$

where $\mathbb{D}_{water}(\mathbf{x})$ denotes the (positive definite and usually diagonalized) water diffusion tensor. This also applies to our choice of q in Section 3.2.

A much simplified situation is encountered when the stress tensor $\mathbb{B}(\mathbf{v})$ has only an isotropic part while the active cell stress is neglected. The above deduction then directly yields, instead of Equation (17),

$$\begin{aligned}\partial_t M =& \nabla \cdot \left(\left(\mathbb{D}_T + \alpha\gamma_2 \frac{s^2}{\lambda}\mathbb{I}_N \frac{M}{\sqrt{K_M^2/X^2 + |\nabla M|^2}} \right) \nabla M \right) + \nabla \cdot (\nabla \cdot \mathbb{D}_T\, M) \\ &+ \nabla \cdot \left(\alpha\gamma_1 \frac{s^2}{\lambda} M \frac{\nabla h}{\sqrt{K_h^2/X^2 + |\nabla h|^2}} \right) + \mu_1 M \left(1 - \frac{M}{K_M}\right)\left(1 - \frac{h}{K_h}\right) + \mu_2 \frac{MW/K_W}{1 + W/K_W}.\end{aligned}$$

For yet another choice of the right hand side in Equation (1) leading in a different but related way to a flux-limited reaction–diffusion–taxis PDE for glioma evolving in a tissue (also under the influence of acidity and vascularization), we refer to [25].

2.2. Endothelial Cells

We turn now to obtaining a macroscopic description for the evolution of ECs. For this purpose, we can reproduce the derivation made in [22], the only difference being that ECs are supposed to respond here to (gradients of) VEGF concentration rather than proliferating glioma cells (Indeed, the latter assumption would be inappropriate in the present context of glioma patterns, where most of the cells are migrating to avoid hypoxic regions, only starting to proliferate when there is enough vascularization.). Therefore, we will only sketch the main steps and refer for details to [22].

We start with the KTE formulation for mesoscopic dynamics of EC distribution function $w(t, \mathbf{x}, \boldsymbol{\vartheta})$:

$$w_t + \nabla_{\mathbf{x}} \cdot (\boldsymbol{\vartheta} w) = \mathcal{L}_w[\eta] w + \mu_w(W, g) w, \tag{18}$$

with turning operator

$$\mathcal{L}_w[\eta] = -\eta(\boldsymbol{\vartheta}, g) w(t, \mathbf{x}, \boldsymbol{\vartheta}) + \int_\Theta \frac{1}{|\Theta|} \eta(\boldsymbol{\vartheta}', g) w(t, \mathbf{x}, \boldsymbol{\vartheta}') d\boldsymbol{\vartheta}', \tag{19}$$

involving a uniform turning kernel and the turning rate

$$\eta(\boldsymbol{\vartheta}, g) = \eta_0 e^{-a(g)D_t g} \tag{20}$$

depending upon the pathwise gradient $D_t g = g_t + \boldsymbol{\vartheta} \cdot \nabla g$ of VEGF concentration. The coefficient function $a(g)$ takes into account the way in which ECs perceive VEGF and respond to it, correspondingly adapting their turning. Following [22], we choose $a(g) = \chi_a \frac{K_R}{(K_R + g/K_g)^2}$, with $\chi_a, K_R > 0$ constants. This corresponds to the rate of change of the expression $y^*(g) = \frac{g/K_g}{g/K_g + K_R}$ representing the equilibrium of EC receptor binding dynamics to g; the constant χ_a scales changes in the turning rate per unit of change in dy^*/dt.

The coefficient $\mu_w(W, g)$ in the proliferation term is chosen as

$$\mu_w(W, g) = \mu_W \left(1 - \frac{W}{K_W}\right) \frac{g}{K_g}, \tag{21}$$

with $\mu_W, K_W, K_g > 0$ constants representing EC growth rate, EC carrying capacity, and maximum amount of VEGF, respectively.

A parabolic scaling $t \rightsquigarrow \varepsilon^2 t$, $\mathbf{x} \rightsquigarrow \varepsilon \mathbf{x}$ performed in the usual way in combination with a Hilbert expansion $w = w_0 + \epsilon w_1 + \epsilon^2 w_2 + \ldots$, a linearization of η, and the assumption that EC proliferation is much slower than migration then leads to the reaction–diffusion–chemotaxis PDE for the leading term in the (macroscopic) Hilbert expansion $W = W_0 + \epsilon W_1 + \epsilon^2 W_2 + \ldots$ (for details, compare with [22]):

$$\partial_t W_0 - \nabla \cdot (\mathbb{D}_{\mathbb{EC}} \nabla W_0) + \nabla \cdot (\chi_a(g) W_0 \nabla g) = \mu_w(W_0, g) W_0, \tag{22}$$

where $\mathbb{D}_{\mathbb{EC}}(\mathbf{x}) := \frac{\sigma^2}{N\eta_0} \mathbb{I}_N$ and $\chi_a(g) := \frac{\sigma^2 a(g)}{N} \mathbb{I}_N = \eta_0 a(g) \mathbb{D}_{\mathbb{EC}}(\mathbf{x})$.

In the sequel, we will (formally) approximate the evolution of W by that of its leading term W_0 and will use the notation W instead of W_0.

2.3. Full Macroscopic System

Equations (17) and (22) are coupled with the following equations set directly on the macroscopic scale and describing the dynamics of VEGF and acidity:

$$g_t = D_g \Delta g + \gamma_g \frac{M \frac{h}{K_h}}{M + K_M} - \zeta_g g \frac{W}{K_W}, \tag{23}$$

$$h_t = D_h \Delta h + \gamma_h \frac{M}{K_M + M} - \zeta_h h \frac{W}{K_W}, \tag{24}$$

where, D_i, γ_i and ζ_i , for $i = h, g$, are positive constants representing diffusion coefficients, production, and uptake rates for the involved quantities.

The above PDE system needs to be supplied with initial conditions; they will be addressed in Section 3. Furthermore, since we are interested in the solution behavior inside a bounded region (representing e.g., a slice of a histologic sample), we restrict our equations (hitherto written for $\mathbf{x} \in \mathbb{R}^N$) to a bounded domain $\Omega \subset \mathbb{R}^N$ and consider no-flux boundary conditions for M, W, g, h. They are naturally assumed for g, h and can be obtained (at least for W) during the upscaling process, as detailed in [23].

3. Numerical Simulations

This section is dedicated to numerical simulations of the macroscopic system obtained in Section 2 for the quantities M, W, g, h.

3.1. Nondimensionalization and Choice of Parameters

We consider the following rescalings of the hitherto dimensional quantities:

$$\tilde{M} := \frac{M}{K_M}, \quad \tilde{h} := \frac{h}{K_h}, \quad \tilde{W} := \frac{W}{K_W}, \quad \tilde{g} := \frac{g}{K_g}, \quad \tilde{t} := \mu_1 t, \quad \tilde{x} := x\sqrt{\frac{\mu_1}{D_h}},$$
$$\tilde{\mathbb{D}}_T := \frac{\mathbb{D}_T}{D_h}, \quad \tilde{\mathbb{D}}_{EC} := \frac{\mathbb{D}_{EC}}{D_h}, \quad \tilde{D}_g := \frac{D_g}{D_h}, \quad \tilde{D}_s = \frac{s^2}{\lambda D_h}, \quad \tilde{\mu}_c := \frac{\mu_2}{\mu_1}, \quad \tilde{\mu}_e := \frac{\mu_W}{\mu_1},$$
$$\tilde{\chi}_W := \chi_a \eta_0, \quad \tilde{\gamma}_g := \frac{\gamma_g}{\mu_1 K_g}, \quad \tilde{\zeta}_g := \frac{\zeta_g}{\mu_1}, \quad \tilde{\gamma}_h := \frac{\gamma_h}{\mu_1 K_h}, \quad \tilde{\zeta}_h := \frac{\zeta_h}{\mu_1}, \quad X := \sqrt{\frac{D_h}{\mu_1}},$$
$$\tilde{\gamma}_1 := \gamma_1 X, \quad \tilde{\gamma}_2 := \gamma_2 X, \quad \tilde{\phi}(\tilde{h}, \tilde{M}) := \frac{\tilde{\gamma}_1 \nabla_{\tilde{x}} \tilde{h}}{\sqrt{1 + |\nabla_{\tilde{x}} \tilde{h}|^2}} + \frac{\tilde{\gamma}_2 \nabla_{\tilde{x}} \tilde{M}}{\sqrt{1 + |\nabla_{\tilde{x}} \tilde{M}|^2}}.$$

After dropping the tildes for simplicity of notation, we therewith get the following nondimensionalized system:

$$M_t = \nabla\nabla : (\mathbb{D}_T M) + \alpha \nabla \cdot ((D_s \mathbb{I}_N - \mathbb{D}_T)\, \phi(h, M) M) + M(1 - M)(1 - h) + \mu_c \frac{MW}{1 + W} \tag{25a}$$
$$W_t = \nabla \cdot (\mathbb{D}_{EC} \nabla W) - \nabla \cdot \left(\chi_W \frac{K_R}{(K_R + g)^2} \mathbb{D}_{EC} W \nabla g \right) + \mu_e g W (1 - W) \tag{25b}$$
$$h_t = \nabla h + \gamma_h \frac{M}{1 + M} - \zeta_h h W \tag{25c}$$
$$g_t = D_g \nabla g + \gamma_g \frac{Mh}{1 + M} - \zeta_g g W, \tag{25d}$$

whose parameters are given by the above scalings and the values provided in Table 1.

Table 1. Parameters (dimensional quantities).

Parameter	Meaning	Value	Reference
K_M	glioma carrying capacity	0.3–0.8 cells/μm^2	this work, [35]
K_h	acidity threshold for cancer cell death	$10^{-6.4}$ mol/L	[36]
s	speed of glioma cells	15–20 μm/h	[37,38]
λ	turning frequency coefficient	360/h	[26,39]
γ_h	proton production rate	3.6×10^{-6} mol/(L·h)	this work, [40]
ζ_h	proton removal rate	3.6×10^{-5}–3.6×10^{-4}/h	this work
D_h	acidity diffusion coefficient	1.8×10^2–3.6×10^4 μm^2/h	this work, [17]
μ_1	glioma growth/decay rate, influenced by acidity	$(4.16–8.3) \times 10^{-3}$/h	[41,42]
μ_2	glioma growth rate, influenced by ECs	$(3–3.95) \times 10^{-2}$/h	this work
α	advection constant	10^3	[23]
γ_1	weight coefficient related to acidic stress	3×10^{-4}–3×10^{-5}/μm	this work
γ_2	weight coefficient related to cell population pressure	10^{-4}–10^{-3}/μm	this work
σ	speed of ECs	15–20 μm/h	[22,43]
η_0	turning rate of ECs	36/h	this work
μ_w	EC proliferation rate	$(1.25–2.08) \times 10^{-3}$/h	this work, [22]
χ_a	coefficient of chemotactic sensitivity of ECs	0.72–21.6 h	this work
K_W	carrying capacity of ECs	0.1–0.3 cells/μm^2	this work, [44]
D_g	diffusion coefficient of VEGF	3.6×10^2–1.04×10^5 μm^2/h	[45,46]
K_g	VEGF threshold value	8×10^{-8}–10^{-6} mol/L	this work, [47]
γ_g	VEGF production rate	3.6×10^{-7} mol/(L·h)	[45]
ζ_g	VEGF uptake rate	3.6×10^{-7}–3.6×10^{-6}/h	this work

3.2. Description of Tissue

Typically, the brain structure of each patient is assessed via diffusion tensor imaging (DTI) and the provided water diffusion tensor $\mathbb{D}_{water}$, already occurring in Section 2.1 above in the peanut distribution. The space scale on which glioma patterns are observed is, however, smaller than the best resolution of DTI, which does not go below the size of a voxel (ca. 1 mm^3): pseudopalisades are structures with a medium width of 200–400 µm; for more details, see the introduction of [17] and references therein. Therefore, as in that reference, we use an artificially created tissue with a corresponding water diffusion tensor as introduced in [34], in order to analyze the effect of tissue anisotropy. We consider the water diffusion tensor as

$$\mathbb{D}_{water}(x,y) = \begin{pmatrix} 0.5 - d(x,y) & 0 \\ 0 & 0.5 + d(x,y), \end{pmatrix} \tag{26}$$

where $d(x,y) = 0.25e^{-0.005(x-450)^2} - 0.25e^{-0.005(y-450)^2}$. A combination of uniform and von Mises–Fisher distributions is considered for the orientation distribution of tissue fibers:

$$q(\mathbf{x},\boldsymbol{\theta}) = \frac{\delta}{2\pi} + (1-\delta)\left(\frac{1}{2\pi I_0(k(\mathbf{x}))}\right)\frac{e^{k(\mathbf{x})\varphi_1(\mathbf{x})\cdot\boldsymbol{\theta}} + e^{-k(\mathbf{x})\varphi_1(\mathbf{x})\cdot\boldsymbol{\theta}}}{2} \tag{27}$$

with $\delta \in [0,1]$ being a weighting coefficient; φ_1 denotes the eigenvector corresponding to the leading eigenvalue of $\mathbb{D}_{water}(\mathbf{x})$ and I_0 is the modified Bessel function of first kind of order 0. Furthermore, $\boldsymbol{\theta} = (\cos\xi, \sin\xi)$ for $\xi \in [0, 2\pi]$, and $k(\mathbf{x}) = \kappa \mathrm{FA}(\mathbf{x})$, where $\kappa \geq 0$ describes the sensitivity of cells toward orientation of tissue fibers and

$$FA(\mathbf{x}) = \frac{|\lambda_1 - \lambda_2|}{\sqrt{\lambda_1^2 + \lambda_2^2}}$$

denotes the fractional anisotropy in 2D [34] with λ_i $(i = 1, 2)$ denoting the eigenvalues of $\mathbb{D}_{water}(\mathbf{x})$.

3.3. Initial Conditions

We consider the following initial densities and concentrations for the quantities involved, as illustrated in Figure 1:

$$M(0,\mathbf{x}) = 0.95 \cdot K_M \cdot \left(e^{\frac{-(x-500)^2-(y-500)^2}{2(25)^2}} + e^{\frac{-(x-600)^2-(y-500)^2}{2(20)^2}} + e^{\frac{-(x-300)^2-(y-400)^2}{2(10)^2}} \right) \tag{28a}$$

$$h(0,\mathbf{x}) = 10^{-7} e^{\frac{-(x-500)^2-(y-500)^2}{2(15)^2}} + 10^{-7} e^{\frac{-(x-600)^2-(y-500)^2}{2(10)^2}} + 10^{-6.4} e^{\frac{-(x-300)^2-(y-400)^2}{2(7.5)^2}} \tag{28b}$$

$$g(0,\mathbf{x}) = 10^{-14} e^{\frac{-(x-500)^2-(y-500)^2}{2(15)^2}} + 10^{-12} e^{\frac{-(x-600)^2-(y-500)^2}{2(10)^2}} + 10^{-11} e^{\frac{-(x-300)^2-(y-400)^2}{2(7.5)^2}} \tag{28c}$$

$$W(0,\mathbf{x}) = 0.02 \cdot K_W \cdot sin^{10}(0.002\pi y) \left(e^{\frac{-(x-50)^2}{0.002}} + e^{\frac{-(x-950)^2}{0.002}} \right). \tag{28d}$$

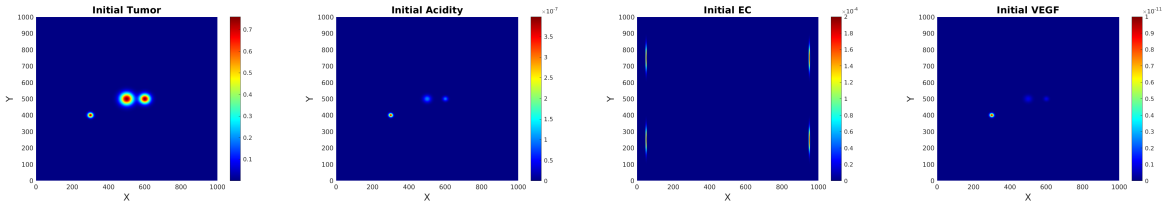

(**a**) Tumor (**b**) Acidity (**c**) ECs (**d**) VEGF

Figure 1. Initial conditions (EC: Endothelial cells, VEGF: Vascular endothelial growth factor).

3.4. Numerical Method

We solve System (25) with no-flux boundary conditions and with the initial data given above on a square domain $[0, 1000] \times [0, 1000]$ (in μm) using a finite difference method. The diffusion parts of acidity (here and subsequently, we mean by "acidity" the concentration of protons, keeping in mind its relationship to the corresponding pH value; the latter usually refers to "acidity" in medical practice), ECs and VEGF are discretized using a standard central difference scheme, while a nonnegativity-preserving discretization scheme, as proposed in [48], is used for the anisotropic diffusion of glioma cells. We apply a first order upwind scheme for the taxis terms in glioma and EC equations. For time discretization, an Implicit-explicit (IMEX) scheme is used for the acidity, EC, and VEFG equations, thereby treating the diffusion parts implicitly and discretizing the taxis and source terms with an explicit Euler method. We use an explicit Euler scheme for each term in the glioma equation.

3.5. Numerical Experiments

We addressed in [17] the case with isotropic tissue ($\delta = 1$), as well as that with anisotropy ($\delta = 0.2$, $k = 3$); here, similar observations can be made in this respect, thus we only consider the latter case. The parameters we use are given in Table 1, with changes correspondingly specified for each scenario.

Experiment 1

To start with, we solve the full System (25) with no-flux boundary conditions and with initial data as in Section 3.3. The results are shown in Figure 2. The garland-shaped glioma pattern forms (and is well visible after 60 simulated days) due to the high proton concentration in its central region, in spite of ECs being attracted by the glioma producing VEGF. In fact, ECs spread over almost the entire domain of simulation, coming from the left and right margins; the EC plot at $t = 60$ days exhibits large densities (except in the narrow central region, where the cells did not yet arrived), a phenomenon known as hyperplasia. Subsequently, ECs have accumulated enough near the tumor to uptake acidity and release nutrients, which leads among others to the tumor cells being able to move away from the acidic area and toward more favorable regions (due to $\gamma_1 \gg \gamma_2$ the influence of acidity dominates the correction of self-diffusion), where they start producing acidity and VEGF. The pseudopalisades develop larger diameters and involve glioma garlands with lower densities. The cancer cells are followed by ECs, which again reduce the proton concentration, thus changing the glioma behavior. The pseudopalisades are disrupted, and at later times, both ECs and glioma cells can repopulate the previously too acidic regions.

Experiment 2

This is the same as **Experiment 1**, but with $\gamma_1 = \gamma_2$, i.e., the flux-limited self-diffusion and pH-taxis being equally weighted. The results are illustrated in Figure 3. The behavior of solution components is qualitatively similar to the previous scenario, except the pseudopalisade-like patterns persist for a longer time; they are succeeded by a more uniform tumor, EC spread occupies the whole domain (also migrating into the formerly most hypoxic areas), and higher cell densities are exhibited.

Experiment 3

Here, we want to assess the effects of extending the model in [17]:

$$M_t = \nabla\nabla : (\mathbb{D}_T M) + \nabla \cdot (G(h) M \mathbb{D}_T \nabla h) + M\,(1 - M)\,(1 - h) \tag{29a}$$

$$h_t = \nabla h + \gamma_h \frac{M}{1 + M} - \zeta_h h, \tag{29b}$$

where $G(h) = \frac{\lambda_1 k_D}{(h+k_D)^2(h+k_D+\lambda_0)}$, $\lambda_0, \lambda_1, k_D > 0$ constants, by dynamics of quantities involved in angiogenesis, i.e., ECs and VEGF. Figure 4 shows differences between glioma density and proton concentration computed with Model (25) and with model versions without vascularization, namely Model (29) (for the left part of Figure 4) and, respectively,

$$M_t = \nabla\nabla : (\mathbb{D}_T M) + \alpha\nabla \cdot ((D_s \mathbb{I}_N - \mathbb{D}_T)\, \phi(h, M) M) + M\,(1 - M)\,(1 - h) \tag{30a}$$

$$h_t = \nabla h + \gamma_h \frac{M}{1 + M} - \zeta_h h. \tag{30b}$$

for the right part of Figure 4.

The plots on the left column exhibit enhanced tumor growth and spread in the presence of ECs and VEGF. Earlier stages feature larger glioma densities (and therewith associated proton concentrations) distributed in a ring-shaped manner, which suggests more pronounced pseudopalisades. At later times, in the presence of vascularization, the tumor cells are not only able to proliferate, but also to reoccupy the formerly overly acidic areas near the center of the simulation domain, while still responding to the spatial distribution of protons. This leads (as observed also in the previous numerical experiments) to patterns no longer having the pseudopalisade-like appearance. Similar effects can be observed in the plots on the right column, although less pronounced, due to the smaller structural difference between the two models compared therein. In fact, at later times, there are only minimal differences between the plots on the left and on the right columns, which suggests that, in the long run, the effects of flux limitation in pH-taxis and additional self-diffusion from Equation (30a) are increasingly diminished in comparison to the simple pH-taxis from Equation (29), most probably because of the diffusion dominance in all these models.

Figure 7 shows differences between 1D tumor and acidity patterns for the model comparison done in the left column of Figure 4 and for two different choices of the diffusion coefficient D_T (which is, in this situation, a scalar function of position): constant (upper row) and involving strong (over two intervals) or milder (at a finite number of positions) degenerations. The plots suggest that the availability of vasculature permits an enhanced tumor spread in regions with higher diffusivity, but also enables invasion in areas where the cells modeled by Model (29) infer strongly degenerate diffusion and therewith associated annihilation of pH-taxis. Moreover, Model (29) predicts high cell accumulation near the interface with highest diffusivity difference, whereas Model (25) eludes such tendency potentially leading to singularities. This is presumably due to the flux-limitations in the taxis and additional self-diffusion terms (for more comments on this issue, we refer to Section 4).

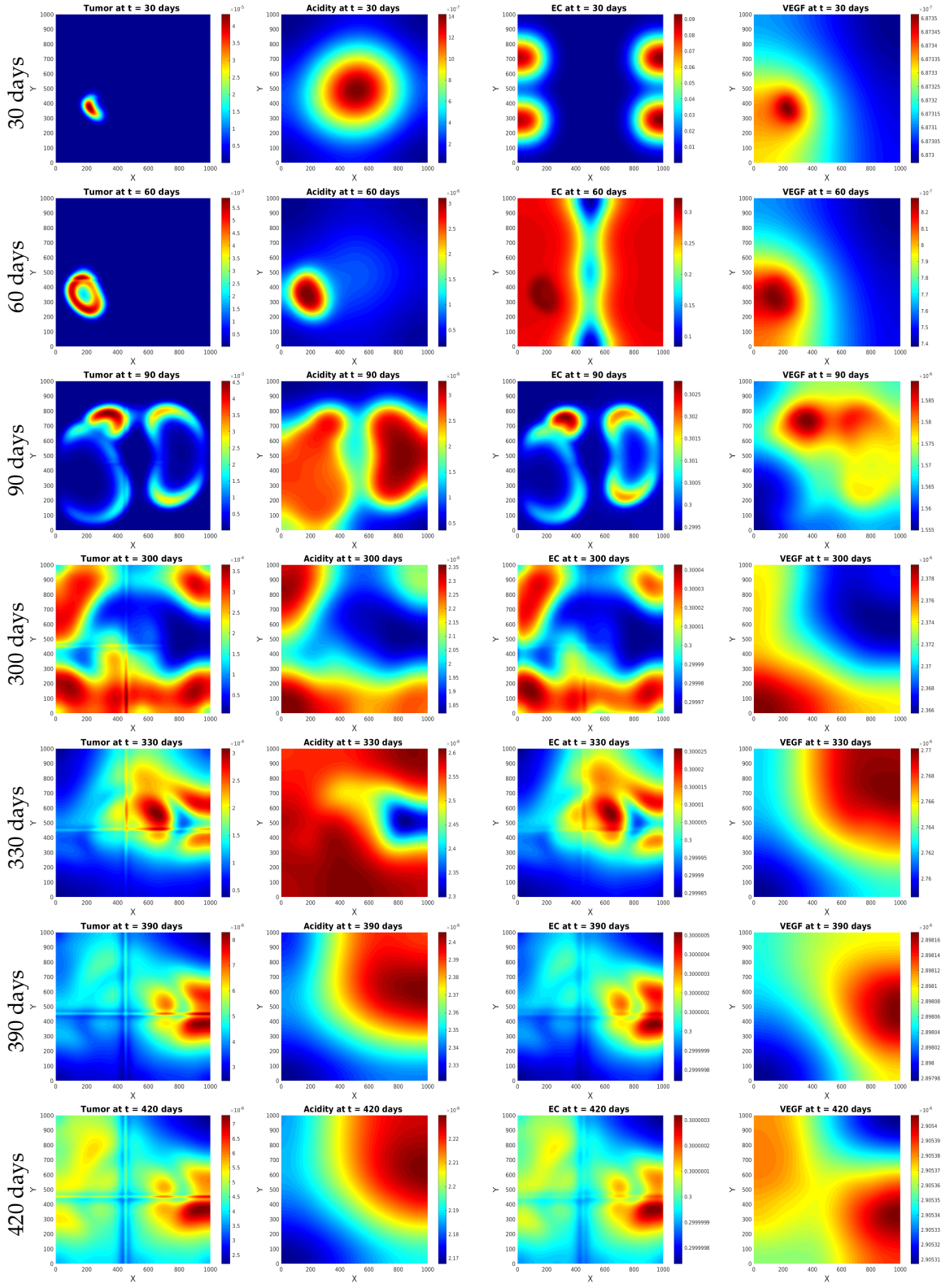

(**a**) Tumor (**b**) Acidity (**c**) ECs (**d**) VEGF

Figure 2. Evolution of the solution components at several times in the framework of Experiment 1 (full model: Model (25)).

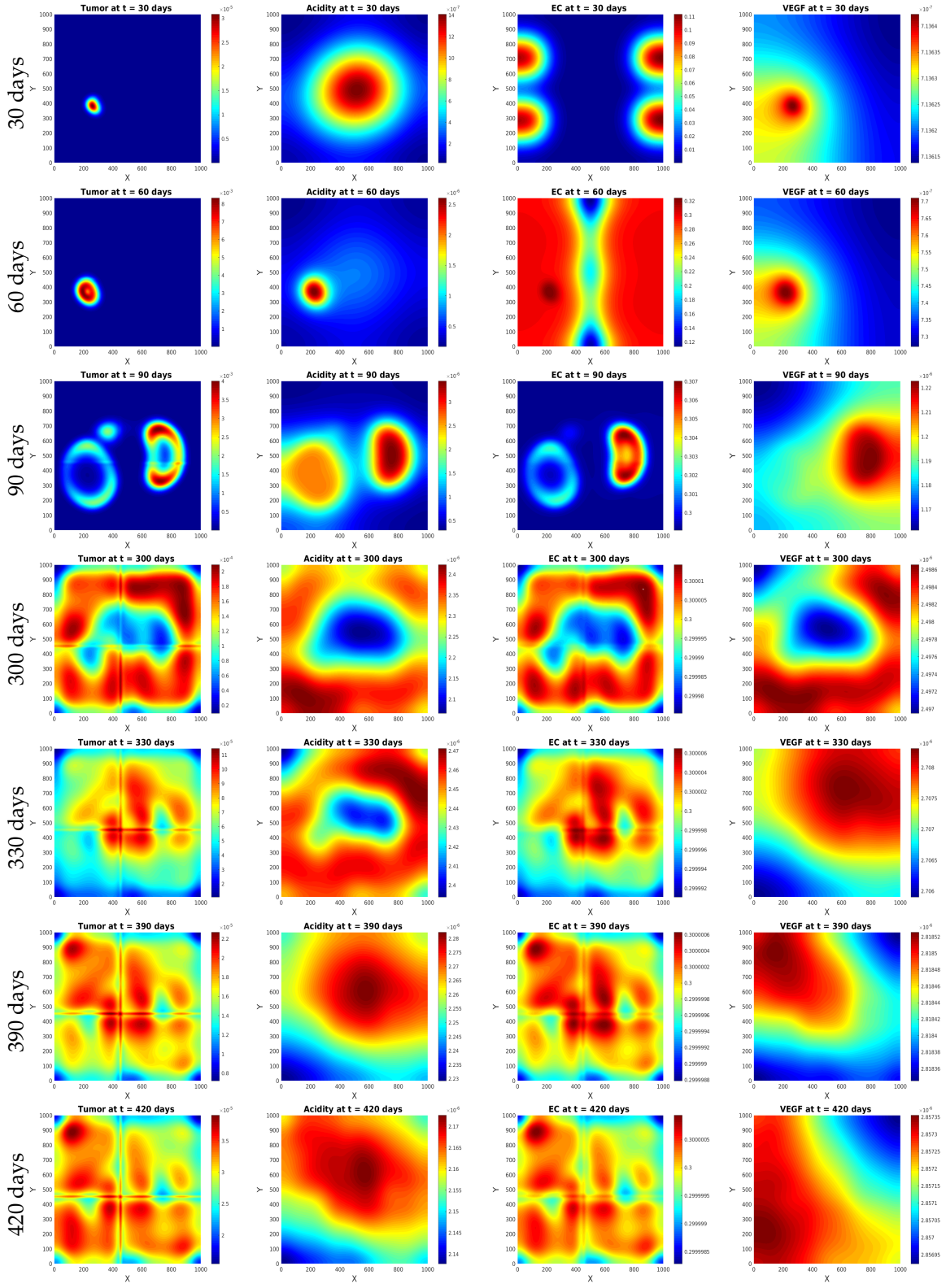

(**a**) Tumor (**b**) Acidity (**c**) ECs (**d**) VEGF

Figure 3. Evolution of the solution components at several times in the framework of Experiment 2 (equally weighted influence of flux-limited repellent pH-taxis and self-diffusion).

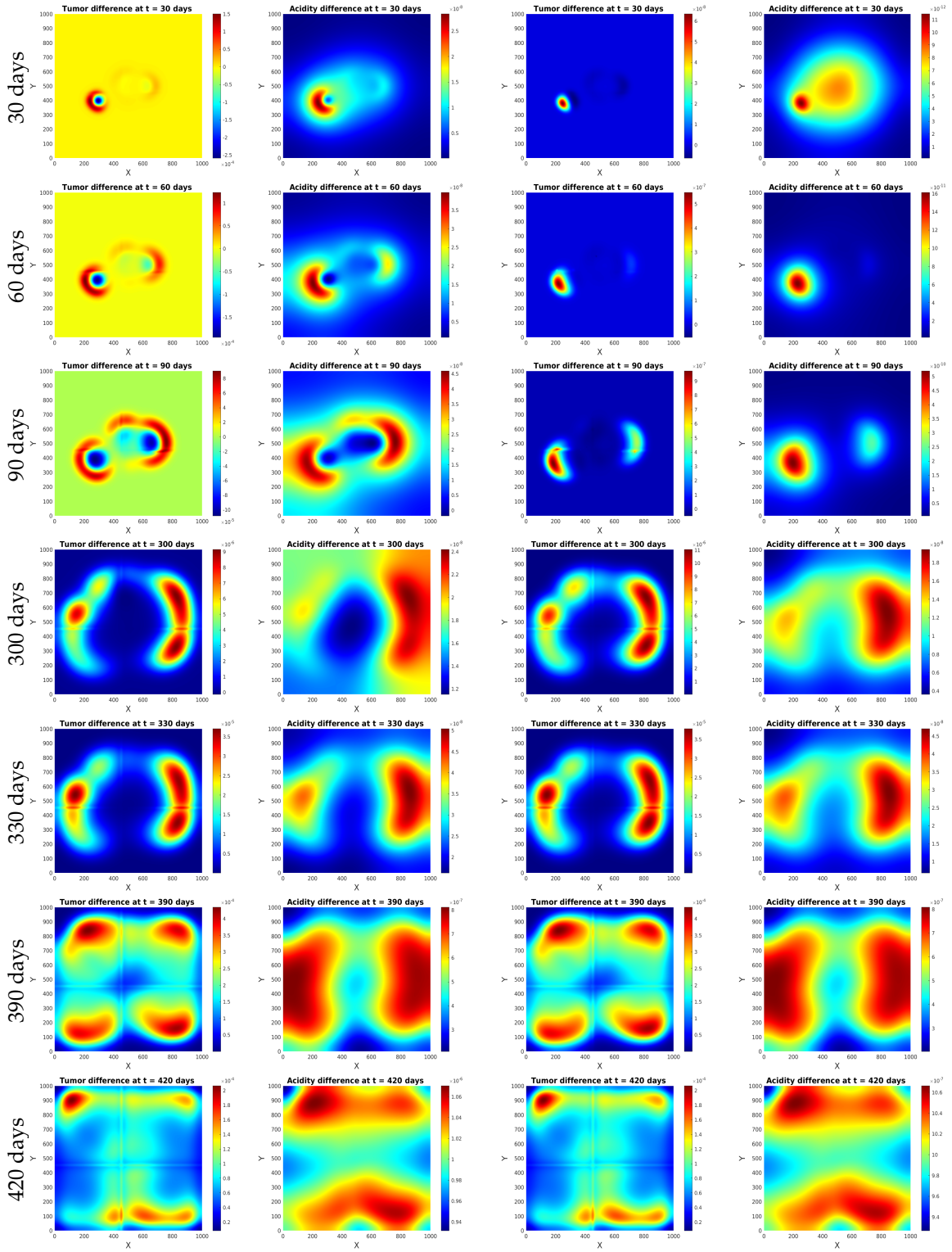

(**a**) Tumor difference (**b**) Acidity difference (**c**) Tumor difference (**d**) Acidity difference

Figure 4. Experiment 3: effect of angiogenesis. Left columns: Difference between tumor density and acidity concentration, as obtained with full System (25), and those computed from the variant Model (29) with proton uptake rate $\zeta_h = 3.6 \times 10^{-8}$/h. Right columns: Same differences, but between computations done with Equation (25) and with Equation (30).

Experiment 4: Effects of flux limitations

We compare the full Model (25) with its counterpart involving in the motility terms only myopic diffusion and pH-taxis without flux saturation, i.e., characterizing glioma density dynamics by

$$M_t = \nabla\nabla : (\mathbb{D}_T M) + \alpha\nabla \cdot (\gamma_1 (D_s \mathbb{I}_N - \mathbb{D}_T) M\nabla h) + M(1-M)(1-h) + \mu_c \frac{MW}{1+W}, \qquad (31)$$

the rest of the equations in Model (25) remaining unchanged. The plots in Figure 5 illustrate the difference between solution components obtained with these two settings, in the above order. At a relatively early stage (30 days), with Equation (25a), there are more glioma cells at the tumor edge, with an obvious preference for moving away from the more acidic, central area. The proton concentration is higher towards the domain margins, and with time passing (plots at 60 days) it becomes consistently larger all over the domain in the model version using Model (31), in which diffusion is dominating over taxis. In that setting, the tumor cell density gets larger as well, which also applies to EC density; although Model (25) features (slightly) more glioma diffusion; however, the flux-limited pH-taxis prevents a faster moving away from acidic regions. Instead, Model (31) ensures a wider spread of glioma, favored by the larger magnitude of the pH-tactic cell fluxes, which lets the tumor cells move faster and therewith produce the attracting VEGF at more locations. After a while (about further 30 days), the previous trend begins to get reversed, as far as glioma density is concerned; the flux limitation keeps the tumor more confined, but the acidity is still diffusing fast, and the expression of VEGF is enhanced, which subsequently leads to hyperplasia, tumor enhancement, and revival of tiny glioma populations at more distant sites (in right half of the simulation domain). At the respective "cancer spots", the cells stay more confined in the flux-limited case, while the variant Model (31) allows the cells to migrate faster (green-yellow margins in tumor difference plot at 90 days). The tumor cells accordingly produce acid and VEGF, attracting even more ECs at their main sites. Much later (300 days), Model (25) predicts larger densities of glioma cells in the center of the domain and near the boundary (the former because of the protons being increasingly removed by arriving ECs, and the latter due to the mutual proliferation support of the two cell types). The setting with Model (31) leads to pseudopalisades with a larger diameter, being preserved for a longer while. Still later (390 days and more), the differences become smaller and smaller in magnitude, while the areas with more or less tumor cells become mixed up, with the pseudopalisades disappearing and giving way to more or less heterogeneous patterns where the glioma cells and ECs are spread over the whole domain. The simulations (observe in particular the plots at 390 and 420 days) also suggest that the motion of ECs is dominated by diffusion (and its limitation near tumor cells) rather than chemotaxis towards VEGF.

Figure 6 illustrates 1D tumor patterns obtained with Model (25) and with Model (31) replacing Equation (25a). Two different choices of the glioma diffusion coefficient $D_T(x)$ (the same as in Figure 7) are considered. Model (25) enables glioma diffusion even in the region where D_T becomes zero, due to the flux-limited self-diffusion, hence the tumor cells can invade a wider area. In both model versions, as a consequence of VEGF availability, more ECs gather in the areas with larger glioma density, which in turn favors proton removal and tumor proliferation, followed again by glioma diffusion. For the strongly degenerating D_T, the setting without flux limitation leads, as in the case investigated in Figure 7, to higher cell accumulations near the interface with highest diffusivity difference, while (as long as M is bounded) the cell flux involving $\phi(h, M)$ in Model (25) is bounded even if the gradients of h and M are not; thus, this model version should be less prone to singular structure formation. It also allows for sharper fronts of the cell mass, as can be seen in the right plot of the second row of Figure 6.

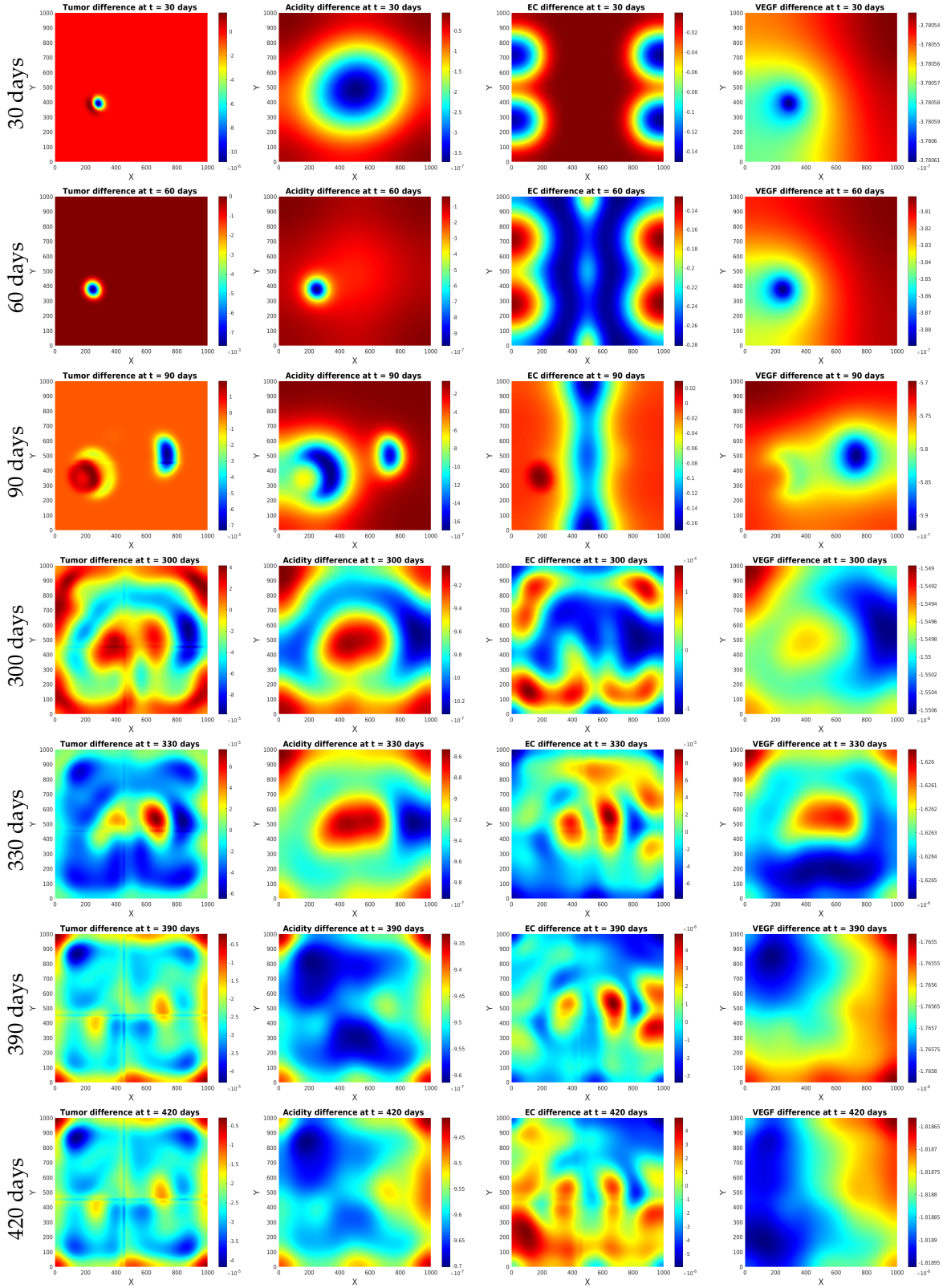

(**a**) Tumor difference (**b**) Acidity difference (**c**) EC difference (**d**) VEGF difference

Figure 5. Experiment 4: effect of flux-limited motility terms. Differences between tumor density and proton concentration computed with Model (25) (in the parameter setting of Experiment 2) and those obtained for a model with glioma motility terms only involving myopic diffusion and pH-taxis without flux saturation (i.e., with glioma dynamics as in Model (31)).

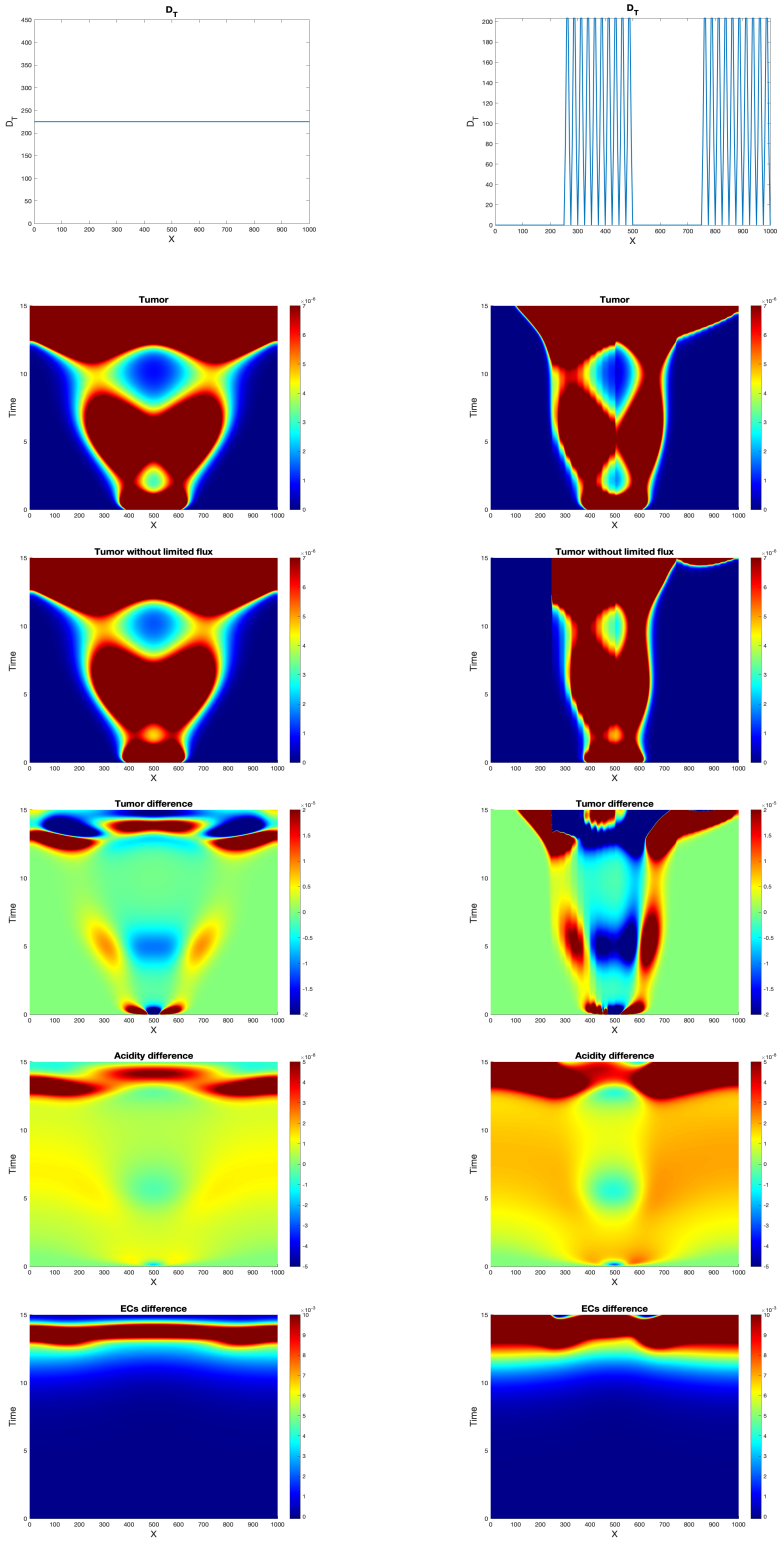

Figure 6. 1D patterns for two different choices of the glioma diffusion coefficient D_T. 2nd row: tumor patterns for Model (25). 3rd row: tumor patterns when Equation (25a) is replaced by Model (31). 4th row: differences between respective patterns in rows 2 and 3. 5th and 6th rows: differences between acidity and EC densities computed with Model (25) and with Model (31) replacing Equation (25a).

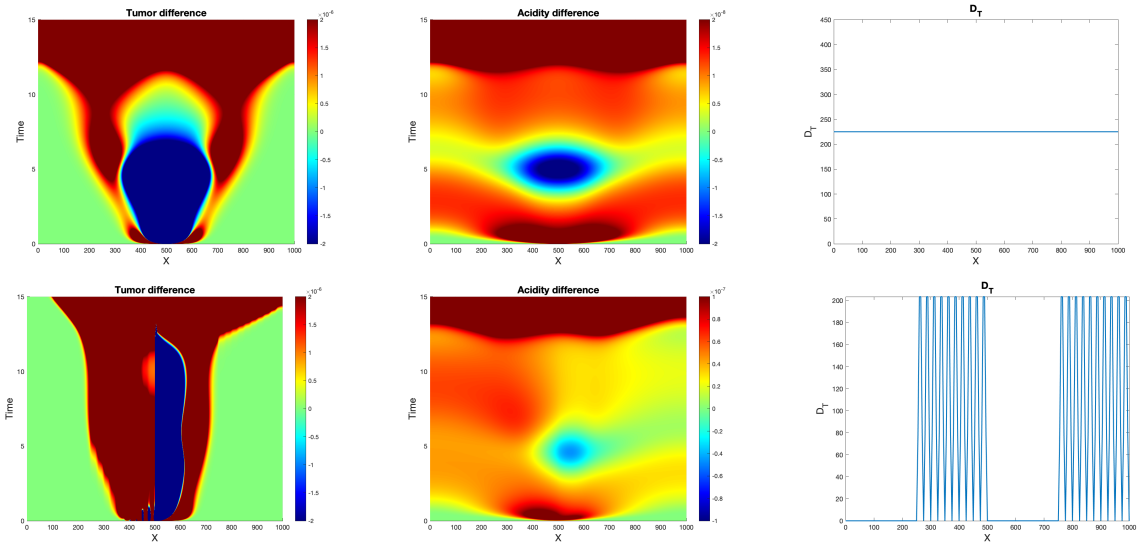

Figure 7. Differences between tumor and acidity patterns (1D) for the model comparison done in the left column of Figure 4 (framework of Experiment 3). Different choices are made for the glioma diffusion coefficient $D_T(x)$, as shown in the rightmost column.

4. Discussion

The vast majority of continuous models for cell migration involve reaction-diffusion(-taxis) PDEs on the macroscopic scale, irrespective to whether those equations were obtained by a direct formulation or a more or less formal deduction from lower scales. Thereby, the diffusion is in some (most often constant) proportion to the density gradient, which is associated to infinite speed of propagation—an unrealistic feature, accompanied by smearing the sharp profile of the cell mass advancing into its surroundings; possible overcrowding effects cannot be properly captured either. These and other issues motivated the introduction of models with flux saturation in this and related contexts; see [49] and citations therein. We also refer to [50,51] for formal and respectively rigorous derivations of chemotaxis models from KTEs, and to [25,52,53] for settings specifically relating to glioma invasion. Among the latter, ref. [25] contains a deduction of macroscopic equations with flux-saturated diffusion, haptotaxis, and chemotaxis; the passage from the mesoscopic KTAP framework to the RDT system is different from the one performed here, yet still formal. Recently, ref. [32] started from a KTE formulation similar to that in [25], hence it is also related to the one in the present work, and obtained by yet another upscaling method (with rigorous convergences) an RDT with myopic diffusion for the zeroth order approximation of the solution. That PDE did not involve flux-limitation, but the equation deduced for the first order correction did.

The model proposed here is still a bottom-up approach connecting subcellular and mesoscopic dynamics with the macroscopic evolution of cell populations in response to cues from the tumor microenvironment, leading to patterns which are qualitatively similar to those observed in histological imaging of glioblastoma. The setting is an extension of the previous one introduced in [17], since it accommodates the description of tumor vascularization in response to hypoxia. The main novelty here is the way of obtaining flux-limited pH-taxis and (supplementary) self-diffusion, namely upon considering on the single cell scale the joint effect of cell stress, chemical gradients, and population pressure to describe forces acting on the cells, cf. Equations (1) and (2). The approach is akin to that employed in [21,23,25], however it involves several modifications, as [21,23] did not contain any flux limitations, while [25] does, but models differently the single cell dynamics (allowing, among others, for non-constant speeds) and does not take into account cell reorientations (by way of a turning operator) in response to local tissue anisotropy and nonlocal orientation distribution of fibers and cells. Our method also differs from [50,51], where the flux limitation stems from the choice of signal response function involved in the turning operator and depending on the directional derivative

of the tactic signals (chemoattractants). We included in Equation (2) only effects of pH-taxis and population pressure, but in modeling glioma migration through a highly anisotropic tissue, one could also involve the influence of its gradients (via macroscopic tissue density, as in [25] or mesoscopic spatial and orientational distribution of tissue fibers, as in [23]). There are two 'sources' of diffusion in our model: the myopic diffusion comes from the description of cell reorientations via the turning operator, while the self-diffusion term with flux limitation originates from Newton's second law in Equations (1) and (2). The latter diffusion part has the effect of eluding diffusion degeneration when the tensor $\mathbb{D}_T$ nullifies as a consequence of the mesoscopic tissue distribution $q(\mathbf{x}, \hat{\mathbf{v}})$ vanishing locally. (Strongly) degenerating myopic diffusion, alone or in combination with taxis have been related to high cell aggregates and possible singularity formation even in lower dimensions [54–56], while flux limitation could alleviate such behavior, at least under certain conditions; see, e.g., [57,58]. This tendency was also observed in Figure 7, in the case with strongly degenerating D_T. Figure 6 showed a sharper tumor cell profile at the interface with large diffusivity drop, while the model without flux limitation generated a more uniform pattern with a tendency of smearing the interface and faster filling the areas of lower cell density. We have to stress, nevertheless, that our deduction of macroscopic PDEs is merely formal; as mentioned above, a rigorous one was done in [32], but for a simplified model and involving only limitation(s) of signal gradient(s) of the form $\frac{\nabla S}{1+|\nabla S|}$ instead of our choice encoded in $\phi(h, M)$.

The obtained macroscopic model is able to reproduce, at least qualitatively, the histological patterns observed in patient biopsies. Indeed, the typical pseudopalisades due to severe hypoxia are formed even when (incipient) angiogenesis is present, followed by a disruption of the 'garlands' as consequence of acidity removal by vasculature (motile ECs) within the pseudopalisades and therewith associated repopulation with tumor cells of the formally acidic sites, which was not or very weakly noticed in simulations of the previous model [17]. The flux limitation does not seem to be necessary for the latter to happen, however it does influence the duration of pattern formation and maintenance, and (to a lesser extent) their appearance. We also noticed (cf. Figures 2 and 3) that the weights assigned to (flux-limited) pH-taxis and self-diffusion affect the patterns in terms of shape, duration, and persistence.

The macroscopic system Model (25) features two types of taxis: a repellent, flux-limited pH-taxis of glioma cells moving in the opposite direction of the proton concentration gradient ∇h, and chemotaxis of endothelial cells following the gradient of VEGF. As such, the setting does not fall into any class of models with multiple taxis as reviewed in [59], since each cell population is performing only one type of taxis, but it raises mathematical questions which are at least partially related to those models. The proton production by tumor cells gives the pH-taxis a direct character, while VEGF, the chemotactic cue of ECs, is produced by glioma cells in presence of acidity; at the same time, glioma proliferation is favorably influenced by ECs. The latter ensure uptake of protons as well as VEGF, hence exert an indirect and also a direct influence on their tactic signal. The mathematical analysis of System (25) with appropriate initial and boundary conditions is far from standard; this is not only due to the myopic diffusion and the nonlinearities arising from the source terms and from couplings, but especially to the flux-limited motility terms in the glioma reaction-diffusion-taxis PDE. Results about well-posedness and long time behavior of solutions to such systems are unknown. We merely provided a couple of examples of simulation-based, 1D pattern assessments in Figures 6 and 7—with no pretension of completeness or rigor, but only for the purpose of giving a flavor of the patterns arising from such model. Beyond that, a traveling wave analysis, particularly of glioma and EC dynamics, would be of interest, both theoretically and from the application viewpoint.

Author Contributions: Conceptualization, C.S. and P.K.; methodology, C.S. and P.K.; software, P.K.; visualization, P.K.; writing—original draft preparation, C.S and P.K.; writing—review and editing, C.S.; supervision, C.S.; funding acquisition, C.S. All authors have read and agreed to the published version of the manuscript.

Funding: P.K. acknowledges funding by DAAD in form of a PhD scholarship. C.S. was funded by BMBF in the project *GlioMaTh* 05M2016.

Conflicts of Interest: The authors declare no conflict of interest.

References

1. Kleihues, P.; Soylemezoglu, F.; Schäuble, B.; Scheithauer, B.; Burger, P. Histopathology, classification and grading of gliomas. *Glia* **1995**, *5*, 211–221. [CrossRef] [PubMed]
2. Perry, A.; Wesseling, P. Histologic classification of gliomas. In *Handbook of Clinical Neurology*; Elsevier: Amsterdam, The Netherlands, 2016; pp. 71–95. [CrossRef]
3. Brat, D.J.; Castellano-Sanchez, A.A.; Hunter, S.B.; Pecot, M.; Cohen, C.; Hammond, E.H.; Devi, S.N.; Kaur, B.; Van Meir, E.G. Pseudopalisades in glioblastoma are hypoxic, express extracellular matrix proteases, and are formed by an actively migrating cell population. *Cancer Res.* **2004**, *64*, 920–927. [CrossRef] [PubMed]
4. Brat, D.J.; Van Meir, E.G. Vaso-occlusive and prothrombotic mechanisms associated with tumor hypoxia, necrosis, and accelerated growth in glioblastoma. *Lab. Investig.* **2004**, *84*, 397–405. [CrossRef] [PubMed]
5. Rong, Y.; Durden, D.L.; Van Meir, E.G.; Brat, D.J. 'Pseudopalisading' necrosis in glioblastoma: A familiar morphologic feature that links vascular pathology, hypoxia, and angiogenesis. *J. Neuropathol. Exp. Neurol.* **2006**, *65*, 529–539. [CrossRef] [PubMed]
6. Wippold, F.; Lämmle, M.; Anatelli, F.; Lennerz, J.; Perry, A. Neuropathology for the neuroradiologist: Palisades and pseudopalisades. *Am. J. Neuroradiol.* **2006**, *27*, 2037–2041. [PubMed]
7. Tate, M.C.; Aghi, M.K. Biology of angiogenesis and invasion in glioma. *Neurotherapeutics* **2009**, *6*, 447–457. [CrossRef]
8. Onishi, M.; Ichikawa, T.; Kurozumi, K.; Date, I. Angiogenesis and invasion in glioma. *Brain Tumor Pathol.* **2011**, *28*, 13–24. [CrossRef]
9. Brat, D.J.; Castellano-Sanchez, A.; Kaur, B.; Van Meir, E.G. Genetic and biologic progression in astrocytomas and their relation to angiogenic dysregulation. *Adv. Anat. Pathol.* **2002**, *9*, 24–36. [CrossRef]
10. Batchelor, T.T.; Reardon, D.A.; de Groot, J.F.; Wick, W.; Weller, M. Antiangiogenic Therapy for Glioblastoma: Current Status and Future Prospects. *Clin. Cancer Res.* **2014**, *20*, 5612–5619. [CrossRef]
11. Zhang, X.; Ding, K.; Wang, J.; Li, X.; Zhao, P. Chemoresistance caused by the microenvironment of glioblastoma and the corresponding solutions. *Biomed. Pharmacother.* **2019**, *109*, 39–46. [CrossRef]
12. Martirosyan, N.; Rutter, E.; Ramey, W.; Kostelich, E.; Kuang, Y.; Preul, M. Mathematically modeling the biological properties of gliomas: A review. *Math. Biosci. Eng.* **2015**, *12*, 879–905. [CrossRef] [PubMed]
13. Alfonso, J.C.L.; Talkenberger, K.; Seifert, M.; Klink, B.; Hawkins-Daarud, A.; Swanson, K.R.; Hatzikirou, H.; Deutsch, A. The biology and mathematical modelling of glioma invasion: A review. *J. R. Soc. Interface* **2017**, *14*, 20170490. [CrossRef] [PubMed]
14. Hatzikirou, H.; Deutsch, A.; Schaller, C.; Simon, M.; Swanson, K. Mathematical Modeling of Glioblastoma Tumor Development: A Review. *Math. Model. Methods Appl. Sci.* **2005**, *15*, 1779–1794. [CrossRef]
15. Cai, Y.; Wu, J.; Li, Z.; Long, Q. Mathematical modelling of a brain tumour initiation and early development: A coupled model of glioblastoma growth, pre-existing vessel co-option, angiogenesis and blood perfusion. *PLoS ONE* **2016**, *11*, e0150296. [CrossRef] [PubMed]
16. Caiazzo, A.; Ramis-Conde, I. Multiscale modelling of palisade formation in gliobastoma multiforme. *J. Theor. Biol.* **2015**, *383*, 145–156. [CrossRef] [PubMed]
17. Kumar, P.; Li, J.; Surulescu, C. Multiscale modeling of glioma pseudopalisades: Contributions from the tumor microenvironment. *arXiv* **2020**, arXiv:2007.05297.
18. Alfonso, J.; Köhn-Luque, A.; Stylianopoulos, T.; Feuerhake, F.; Deutsch, A.; Hatzikirou, H. Why one-size-fits-all vaso-modulatory interventions fail to control glioma invasion: In silico insights. *Sci. Rep.* **2016**, *6*, 37283. [CrossRef]
19. Martínez-González, A.; Calvo, G.; Pérez Romasanta, L.; Pérez-García, V. Hypoxic cell waves around necrotic cores in glioblastoma: A biomathematical model and its therapeutic implications. *Bull. Math. Biol.* **2012**, *74*, 2875–2896. [CrossRef]
20. Bellomo, N.; Bellouquid, A.; Gibelli, L.; Outada, N. *A Quest Towards a Mathematical Theory of Living Systems*; Birkhäuser: Basel, Switzerland, 2017.
21. Chauvière, A.; Hillen, T.; Preziosi, L. Modeling cell movement in anisotropic and heterogeneous network tissues. *Netw. Heterog. Media* **2007**, *2*, 333. [CrossRef]

22. Conte, M.; Surulescu, C. Mathematical modeling of glioma invasion: Acid-and vasculature mediated go-or-grow dichotomy and the influence of tissue anisotropy. *arXiv* **2020**, arXiv:2007.12204.
23. Corbin, G.; Engwer, C.; Klar, A.; Nieto, J.; Soler, J.; Surulescu, C.; Wenske, M. Modeling glioma invasion with anisotropy-and hypoxia-triggered motility enhancement: From subcellular dynamics to macroscopic PDEs with multiple taxis. *arXiv* **2020**, arXiv:2006.12322.
24. Corbin, G.; Hunt, A.; Klar, A.; Schneider, F.; Surulescu, C. Higher-order models for glioma invasion: From a two-scale description to effective equations for mass density and momentum. *Math. Model. Methods Appl. Sci.* **2018**, *28*, 1771–1800. [CrossRef]
25. Dietrich, A.; Kolbe, N.; Sfakianakis, N.; Surulescu, C. Multiscale modeling of glioma invasion: From receptor binding to flux-limited macroscopic PDEs. *arXiv* **2020**, arXiv:2010.03277.
26. Engwer, C.; Hillen, T.; Knappitsch, M.; Surulescu, C. Glioma follow white matter tracts: A multiscale DTI-based model. *J. Math. Biol.* **2015**, *71*, 551–582. [CrossRef] [PubMed]
27. Engwer, C.; Knappitsch, M.; Surulescu, C. A multiscale model for glioma spread including cell-tissue interactions and proliferation. *Math. Biosci. Eng.* **2016**, *13*, 443–460. [CrossRef]
28. Engwer, C.; Hunt, A.; Surulescu, C. Effective equations for anisotropic glioma spread with proliferation: A multiscale approach and comparisons with previous settings. *Math. Med. Biol. A J. IMA* **2016**, *33*, 435–459. [CrossRef]
29. Hillen, T. M 5 mesoscopic and macroscopic models for mesenchymal motion. *J. Math. Biol.* **2006**, *53*, 585–616. [CrossRef]
30. Hillen, T.; Painter, K.J. Transport and anisotropic diffusion models for movement in oriented habitats. In *Dispersal, Individual Movement and Spatial Ecology*; Springer: Berlin/Heidelberg, Germany, 2013; pp. 177–222.
31. Hunt, A.; Surulescu, C. A multiscale modeling approach to glioma invasion with therapy. *Vietnam. J. Math.* **2017**, *45*, 221–240. [CrossRef]
32. Zhigun, A.; Surulescu, C. A novel derivation of rigorous macroscopic limits from a micro-meso description of signal-triggered cell migration in fibrous environments. *arXiv* **2020**, arXiv:2010.04148.
33. Aylaj, B.; Bellomo, N.; Chouhad, N.; Knopoff, D. On the Interaction Between Soft and Hard Sciences: The Role of Mathematical Sciences. *Vietnam. J. Math.* **2020**. [CrossRef]
34. Painter, K.; Hillen, T. Mathematical modelling of glioma growth: The use of Diffusion Tensor Imaging (DTI) data to predict the anisotropic pathways of cancer invasion. *J. Theor. Biol.* **2013**, *323*, 25–39. [CrossRef] [PubMed]
35. Available online: https://bionumbers.hms.harvard.edu/bionumber.aspx?s=n&v=0&id=108941 (accessed on 17 July 2020).
36. Webb, B.; Chimenti, M.; Jacobson, M.; Barber, D. Dysregulated pH: A perfect storm for cancer progression. *Nat. Rev. Cancer* **2011**, *11*, 671–677. [CrossRef] [PubMed]
37. Diao, W.; Tong, X.; Yang, C.; Zhang, F.; Bao, C.; Chen, H.; Liu, L.; Li, M.; Ye, F.; Fan, Q.; et al. Behaviors of glioblastoma cells in in vitro microenvironments. *Sci. Rep.* **2019**, *9*, 1–9. [CrossRef] [PubMed]
38. Prag, S.; Lepekhin, E.; Kolkova, K.; Hartmann-Petersen, R.; Kawa, A.; Walmod, P.; Belman, V.; Gallagher, H.; Berezin, V.; Bock, E.; et al. NCAM regulates cell motility. *J. Cell Sci.* **2002**, *115*, 283–292.
39. Sidani, M.; Wessels, D.; Mouneimne, G.; Ghosh, M.; Goswami, S.; Sarmiento, C.; Wang, W.; Kuhl, S.; El-Sibai, M.; Backer, J.; et al. Cofilin determines the migration behavior and turning frequency of metastatic cancer cells. *J. Cell Biol.* **2007**, *179*, 777–791. [CrossRef]
40. Martin, G.; Jain, R. Noninvasive Measurement of Interstitial pH Profiles in Normal and Neoplastic Tissue Using Fluorescence Ratio Imaging Microscopy. *Cancer Res.* **1994**, *54*, 5670–5674.
41. Stein, A.; Demuth, T.; Mobley, D.; Berens, M.; Sander, L. A mathematical model of glioblastoma tumor spheroid invasion in a three-dimensional in vitro experiment. *Biophys. J.* **2007**, *92*, 356–365. [CrossRef]
42. Eikenberry, S.; Sankar, T.; Preul, M.; Kostelich, E.; Thalhauser, C.; Kuang, Y. Virtual glioblastoma: Growth, migration and treatment in a three-dimensional mathematical model. *Cell Prolif.* **2009**, *42*, 511–528. [CrossRef]
43. Czirok, A. Endothelial cell motility, coordination and pattern formation during vasculogenesis. *Wiley Interdiscip. Rev. Syst. Biol. Med.* **2013**, *5*, 587–602. [CrossRef]
44. Available online: https://www.lab.anhb.uwa.edu.au/mb140/MoreAbout/Endothel.htm (accessed on 22 June 2020).

45. Plank, M.; Sleeman, B.; Jones, P. A mathematical model of tumour angiogenesis, regulated by vascular endothelial growth factor and the angiopoietins. *J. Theor. Biol.* **2004**, *229*, 435–454. [CrossRef]
46. Shamsi, M.; Saghafian, M.; Dejam, M.; Sanati-Nezhad, A. Mathematical modeling of the function of Warburg effect in tumor microenvironment. *Sci. Rep.* **2018**, *8*, 1–13. [CrossRef] [PubMed]
47. Gevertz, J.L.; Torquato, S. Modeling the effects of vasculature evolution on early brain tumor growth. *J. Theor. Biol.* **2006**, *243*, 517–531. [CrossRef] [PubMed]
48. Weickert, J. *Anisotropic Diffusion in Image Processing*; Teubner Stuttgart: Stuttgart, Germany, 1998; Volume 1.
49. Burini, D.; Chouhad, N. A multiscale view of nonlinear diffusion in biology: From cells to tissues. *Math. Model. Methods Appl. Sci.* **2019**, *29*, 791–823. [CrossRef]
50. Bellomo, N.; Bellouquid, A.; Nieto, J.; Soler, J. Multiscale biological tissue models and flux-limited chemotaxis for multicellular growing systems. *Math. Models Methods Appl. Sci.* **2010**, *20*, 1179–1207. [CrossRef]
51. Perthame, B.; Vauchelet, N.; Wang, Z. The Flux Limited Keller-Segel System; Properties and Derivation from Kinetic Equations. *arXiv* **2018**, arXiv:1801.07062.
52. Conte, M.; Casas-Tintò, S.; Soler, J. Modeling invasion patterns in the glioblastoma battlefield. *bioRxiv* **2020**.
53. Kim, Y.; Lawler, S.; Nowicki, M.; Chiocca, E.; Friedman, A. A mathematical model for pattern formation of glioma cells outside the tumor spheroid core. *J. Theor. Biol.* **2009**, *260*, 359–371. [CrossRef]
54. Hillen, T.; Painter, K.; Winkler, M. Anisotropic diffusion in oriented environments can lead to singularity formation. *Eur. J. Appl. Math.* **2013**, *24*, 371–413. [CrossRef]
55. Winkler, M.; Surulescu, C. Global weak solutions to a strongly degenerate haptotaxis model. *Comm. Math. Sci.* **2017**, *15*, 1581–1616. [CrossRef]
56. Winkler, M. Singular structure formation in a degenerate haptotaxis model involving myopic diffusion. *J. Math. Pures Appl.* **2018**, *112*, 118–169. [CrossRef]
57. Bellomo, N.; Winkler, M. Finite-time blow-up in a degenerate chemotaxis system with flux limitation. *Trans. Am. Math. Soc. Ser. B* **2017**, *4*, 31–67. [CrossRef]
58. Bellomo, N.; Winkler, M. A degenerate chemotaxis system with flux limitation: Maximally extended solutions and absence of gradient blow-up. *Comm. Partial. Differ. Equ.* **2017**, *42*, 436–473. [CrossRef]
59. Kolbe, N.; Sfakianakis, N.; Stinner, C.; Surulescu, C.; Lenz, J. Modeling multiple taxis: Tumor invasion with phenotypic heterogeneity, haptotaxis, and unilateral interspecies repellence. *Discret. Contin. Dyn. Syst. B* **2020**. [CrossRef]